EFFECT OF MAGNESIUM CONTENT ON PRECIPITATION BEHAVIOR OF TiN-CONTAINING INCLUSIONS IN HIGH-TITANIUM HIGH-STRENGTH STEEL

Yong Wan, Xuejian Zhang, Chuansheng Tang, Yonghong Wen [ORCID], Lijie Tian and Mingqi Liu

Key Laboratory of Metallurgical Emission Reduction & Resources Recycling (Anhui University of Technology), Ministry of Education, Ma'anshan 243002, Anhui, China

School of Metallurgical Engineering, Anhui University of Technology, Ma'anshan 243002, Anhui, China

Abstract

High-temperature melting experiments (1600 °C), metallographic microscopy and scanning electron microscopy were used to investigate the morphology, quantity and size of TiN in the center of high-titanium high-strength steels under different Mg content (0 wt.% → 0.0023 wt.%). The results showed that based on thermodynamic calculations regarding the aluminum-magnesium content relationship during deoxidation product formation, significant amounts of $MgAl_2O_4$ are generated even with trace amounts of Mg present in the tested steel. The solidification structures of all tested steels are equiaxed grains when the solidification cooling rate is 0.17 °C/s. The average size of equiaxial grain in the tested steels decreased from 320 to 271 µm, 195 and 101 µm as the Mg content increased from 0 to 0.0007 wt.%, 0.00014 and 0.0023 wt.%, respectively. MgO and $MgAl_2O_4$ precipitate before TiN and have a small lattice mismatch with TiN (0.02 and 5.03%, respectively). As the Mg content in the steel increased from 0 to 0.0007 wt.%, 0.0014 and 0.0023 wt.%, the areal density of TiN in the tested steels increased from 44.4 to 102.4 No./mm^2, 129.4 and 144.2 No./mm^2, the maximum size of TiN particles decreased from 16.5 to 10.4 µm, 9.8 and 9.3 µm, the average size of TiN decreased from 9.1 to 4.2 µm, 3.3 and 3.1 µm, and the proportion of TiN precipitated at the grain boundaries decreases from 22.7 to 16.8%, 14.5 and 14.8%, respectively.

Keywords: magnesium treatment, high-titanium high-strength steel, equiaxed grain, TiN, heterogeneous nucleation

Introduction

High-strength steel is extensively utilized in automotive, aerospace and construction industries due to its exceptional strength and durability.[1,2] High-strength steel achieves its remarkable properties primarily through complex microalloying with elements such as Nb, V and Ti, which are strong carbon (nitrogen) compound formers capable of forming stable precipitates. These precipitates refine the grain structure and impede dislocation movement, consequently enhancing steel yield and tensile strength.[3] Among the various types of microalloyed high-strength steels, microalloying of titanium has shown the most significant effect on material strength. Also, it offers a distinct advantage in terms of raw material costs. Thus, microalloying of titanium is prevalently regarded as the principal approach for grain refinement and strength enhancement.[4,5] However, large TiN particles (> 10 µm) precipitate quickly form in the center of the steel during the continuous casting process for a high Ti content in the steel. These large, hard TiN particles diminish the toughness, weldability, and fatigue limit of high-strength steel and lead to stress concentration, which accelerates the initiation and propagation of cracks, causing a notable reduction in the central region strength of the rolled product.[6–8] Numerous studies have been conducted to investigate this issue through experiments and establish models for calculating TiN precipitation during the solidification process of molten steel. It has been found that a considerable amount of TiN precipitates within the solid-liquid two-phase zone due to the gradual enrichment and segregation of Ti and N atoms at the solidification front.[9–13] Therefore, avoiding the formation of large TiN particles in the center of solidified steel is a critical issue that needs to be addressed urgently in the industrial production of Ti-

microalloyed high-strength steel. Unfortunately, few reports exist on refining the large TiN particles in the center of high-titanium high-strength steel.

In recent years, extensive research has been conducted on adding trace amounts of magnesium to steel to manipulate the growth of inclusions. During the cooling and solidification process of molten steel, high-melting-point magnesium oxides can stably exist and provide heterogeneous nucleation sites for the secondary phase particles in molten steel, thereby refining the solidification structure. Jo[14] and Ohta[15] investigated the thermodynamic dominance region diagram of Mg–Al–O inclusions in molten steel containing 40%Ni and 20%Cr, revealing that only a small quantity of magnesium can modify Al_2O_3. Yang[16] et al. investigated ladle furnace (LF) refining techniques applied to low carbon aluminum killed (LCAK) steel and calculated a thermodynamic diagram illustrating the relationship between Mg, Al and O in molten steel. Their findings indicated that when [Al] content reached 0.04%, approximately 0.5 ppm [Mg] was required to convert Al_2O_3 into $MgAl_2O_4$. Wang et al.,[17] through their experimentation with H13 steel subjected to magnesium treatment, found that when the magnesium content was below 12 ppm, the inclusions present were primarily composed of Al_2O_3 and $MgAl_2O_4$. As the amount of added magnesium increased, so did the number of $MgAl_2O_4$ in the steels. Once reaching a concentration level at around 28 ppm, all existing inclusions transformed completely into $MgAl_2O_4$. Further increase in magnesium content led to precipitation of MgO. Additionally, it was observed that inclusion sizes larger than 2 μm decreased while those around 1 μm increased. Isobe[18] and Kimura[19] investigated the effect of Mg and Ti on the formation of equiaxed grains. They found that adding Mg promotes the formation of equiaxed grain, with a significant increase in the rate of equiaxed grain formation as Mg content increases. Qu et al.[20] found that magnesium treatment in Ti-bearing peritectic steel consistently led to the presence of high-temperature oxides, such as $MgAl_2O_4$ or MgO, in molten steel. This treatment resulted in a 49% decrease in the average size of TiN particles post-treatment compared to pre-treatment. This indicated that the $MgAl_2O_4$ or MgO particles formed after magnesium treatment promote the heterogeneous nucleation of TiN, providing nucleation sites for the refinement of high-temperature δ-ferrite. Previous studies on homogeneous and heterogeneous nucleation behavior of TiN in steel mainly focused on medium to low titanium steels under fast cooling conditions such as air or water. Consequently, these findings cannot directly guide the control over the size of TiN refinement in the central region during continuous casting for refined high-titanium steels. Therefore, this study focuses on high-titanium high-strength steel as the research subject to investigate the influence of varying magnesium content on the type, quantity and size of TiN precipitation in the steel after slow solidification cooling process. The aim is to provide a scientific basis and practical

Figure 1. High-temperature Muffle furnace (T-1700VCB).

guidance for precise control of TiN in the billet central region during continuous casting.

Experimental Materials and Methods

Four high-titanium high-strength steels with varying magnesium content were melted in a high-temperature muffle furnace at a temperature of 1600 °C and were cast into 1.2 kg ingots. The high-temperature muffle furnace (T-1700VCB) was shown in Fig. 1. When the temperature reached 1600 °C in the muffle furnace, the tested steel completely melted. The first step involved deoxygenating the molten steel by adding silicon and aluminum. The second step was the introducting magnesium–aluminum alloy into the molten steel, and the third step involved the addition of titanium to the molten steel. Then, the tested steels were cooled in the furnace to room temperature (cooling rate of 0.17 °C/s). The chemical composition of four tested steels was detected by an inductively coupled plasma optical emission spectrometer, and the content of N and O was detected by a TC500 nitrogen and oxygen analyzer. Swarf was cut from four tested steels, and the magnesium content was determined using chemical analysis method. Their chemical compositions were listed in Table 1. After the tested steel ingots were cooled to room temperature, the crucible was taken out from the high-

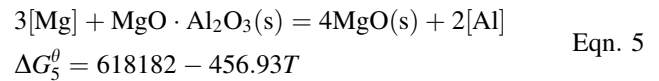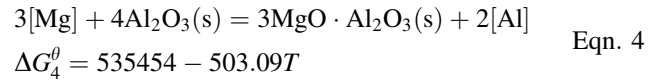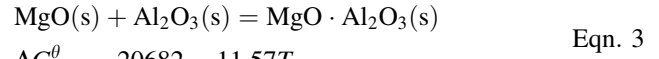**Table 1. Chemical Composition of Tested Steels (wt.%)**

No.	C	Si	Mn	P	S	Al	Ti	Mg	T[O]	N
1	0.078	0.0142	1.654	0.0116	0.0022	0.057	0.10	0	0.0007	0.0123
2	0.074	0.078	1.643	0.0107	0.0021	0.049	0.10	0.0007	0.0013	0.0126
3	0.070	0.074	1.657	0.0111	0.0019	0.056	0.11	0.0014	0.0006	0.0140
4	0.082	0.0113	1.651	0.0121	0.0025	0.065	0.12	0.0023	0.0009	0.0133

temperature muffle furnace, then the tested steel ingots ($\Phi 48$ mm $\times$ 80 mm) were taken out from the crucible, as shown in Fig. 2. Wire electrical discharge machining was used to cut the bottom of the tested steel ingots at a height of 15 mm, then took out a $\Phi 18$-mm cylindrical sample in the middle. The $\Phi 18$-mm cylindrical sample was ground, polished and eroded with 4 vol.% nitric acid alcohol solution. The typical morphology and composition of TiN on the etched surface of each sample were observed and analyzed using a scanning electron microscope (JEM-6510). The etched surfaces were continuously observed and photographed using a metallurgical microscope (UCMOS03100KPA). Photoshop software was used to statistically analyze and measure the quantity and size of TiN within each field of view to calculate the TiN density in different size ranges. The TiN density is the total number of TiN divided by the total area. By utilizing the primary chemical reactions responsible for the formation of Mg inclusions and employing the principle of minimizing Gibbs free energy, this study calculates the correlation between Mg and Al content and the equilibrium products of deoxidation. Furthermore, it analyzes the association between Mg inclusions and heterogeneous nucleation of TiN in high-titanium high-strength steels with varying Mg contents.

Experimental Results and Analysis

Thermodynamic Analysis of MgO and MgAl₂O₄ Formation During Mg Deoxidation in the Tested Steels

After adding Mg to molten steel, the chemical reactions involved in the Fe–Mg–Al–O system at 1600 °C and their corresponding standard Gibbs free energy (ΔG^θ) of formation are expressed by Eqns. 1–5.[20-23] Equations 4 and 5 are obtained through a linear combination of Eqns. 1–3. In molten steel, the content of elements other than Fe is relatively low, which conforms to Henry's Law, thus considering molten steel as an ideal solution.

$$2[Al] + 3[O] = Al_2O_3(s)$$
$$\Delta G_1^\theta = -867500 + 222.5T \qquad \text{Eqn. 1}$$

$$[Mg] + [O] = MgO(s)$$
$$\Delta G_2^\theta = -90000 - 82.0T \qquad \text{Eqn. 2}$$

$$MgO(s) + Al_2O_3(s) = MgO \cdot Al_2O_3(s)$$
$$\Delta G_3^\theta = -20682 - 11.57T \qquad \text{Eqn. 3}$$

$$3[Mg] + 4Al_2O_3(s) = 3MgO \cdot Al_2O_3(s) + 2[Al]$$
$$\Delta G_4^\theta = 535454 - 503.09T \qquad \text{Eqn. 4}$$

$$3[Mg] + MgO \cdot Al_2O_3(s) = 4MgO(s) + 2[Al]$$
$$\Delta G_5^\theta = 618182 - 456.93T \qquad \text{Eqn. 5}$$

At 1600 °C equilibrium, the Gibbs free energy (ΔG) for the formation of MgAl₂O₄ and MgO in molten steel within the Fe–Mg–Al–O system can be expressed by Eqns. 6 and 7:

$$\Delta G = \Delta G_4^\theta + RT \ln \frac{a_{(MgAl_2O_4)}^3 \cdot a_{[Al]}^2}{a_{(Al_2O_3)}^4 \cdot a_{[Mg]}^3} \qquad \text{Eqn. 6}$$

$$\Delta G = \Delta G_5^\theta + RT \ln \frac{a_{(MgO)}^4 \cdot a_{[Al]}^2}{a_{(MgAl_2O_4)} \cdot a_{[Mg]}^3} \qquad \text{Eqn. 7}$$

where $a_{(MgAl_2O_4)}$, $a_{(Al_2O_3)}$, $a_{[Al]}$ and $a_{[Mg]}$ denote the activities of MgAl₂O₄, Al₂O₃, MgO, Al and Mg in molten steel, respectively. Herein, $a_{(MgAl_2O_4)} = 1$, $a_{(Al_2O_3)} = 1$ and $a_{(MgO)} = 1$; $w_{[Al]}$ and $w_{[Mg]}$ denote the mass fractions of Al and Mg in molten steel, respectively; $a_{[Al]}$ and $a_{[Mg]}$ can be obtained by Eqns. 8 and 9:

$$a_i = f_i[\%i] \qquad \text{Eqn. 8}$$

$$\lg f_i = \sum_{j=1}^{n} e_i^j [\%i] \qquad \text{Eqn. 9}$$

where i are the elements of Al and Mg; j are the solute elements; f_i denote the activity coefficients of Al and Mg; e_i^j represents the first-order interaction coefficients, the values of which are displayed in Table 2.

The relationship between the Al and Mg content during the formation of different deoxidation inclusions can be derived from Eqns. 4–9:

$$MgAl_2O_4 - Al_2O_3 : [\%Mg] = 3.347 \times 10^{-4}[\%Al] \qquad \text{Eqn. 10}$$

$$MgO - MgOAl_2O_4 : [\%Mg] = 1.253 \times 10^{-2}[\%Al] \qquad \text{Eqn. 11}$$

Based on Eqns. 10 and 11, the relationship between Mg and Al contents and deoxidation inclusions in the tested steel at 1600 °C is shown in Fig. 3. As shown in Fig. 3, deoxidation products are categorized into three sections:

Figure 2. Tested steel ingots: (a) 0 wt.% Mg; (b) 0.0007 wt.% Mg; (c) 0.0014 wt.% Mg; (d) 0.0023 wt.% Mg.

Table 2. e_{Al}^{j} and e_{Mg}^{j} in Molten Steel at 1600 °C [24,25]

Element	C	Si	Mn	P	S	Al	Ti	Mg	O	N
Al	0.091	0.0056	0.0035	0.033	0.03	0.045	0.004	− 1.98	− 6.6	− 0.053
Mg	−0.24	−0.088	0.024	–	−1.38	−0.12	−0.51	− 0.047	− 289	–
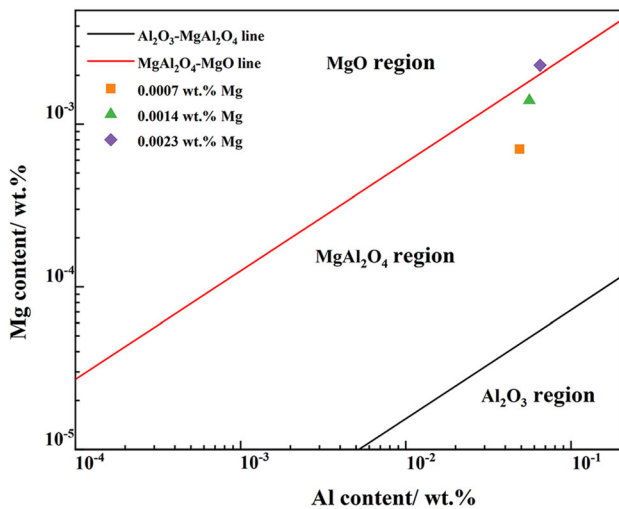
Figure 3. Relationship between magnesium content and aluminum content in the tested steels at 1600°C.

Al_2O_3, $MgAl_2O_4$ and MgO. At 1600 °C, the composition of No. 2 steels (0.0007 wt.% Mg) and No. 3 (0.0014 wt.% Mg) is situated in the formation region of $MgAl_2O_4$, resulting in a large amount of $MgAl_2O_4$. The composition of No. 4 steel (0.0023 wt.% Mg) lies in the MgO region, resulting in a substantial formation of $MgAl_2O_4$ and a minor amount of MgO.
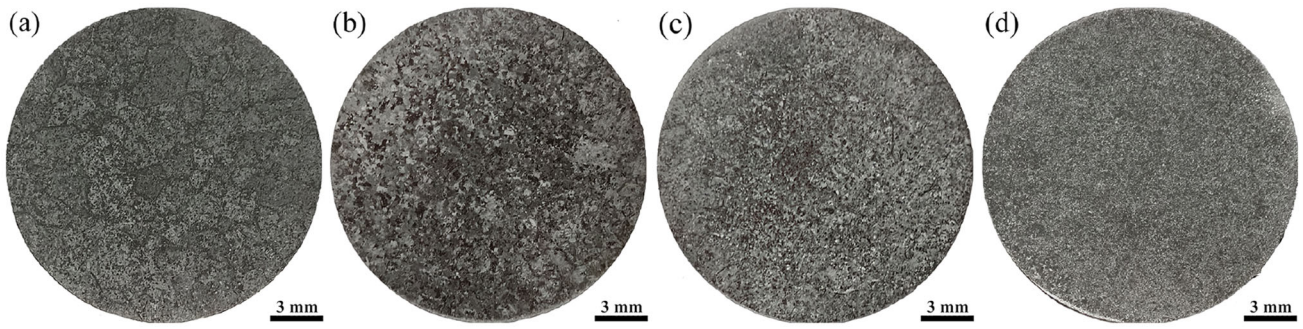
Solidification Structure of Tested Steels with Different Magnesium Contents

The statistical results of the solidification structure and average grain size of tested steels with varying Mg content are shown in Figs. 4 and 5. From Fig. 4, the solidification structures of tested steels with varying Mg contents are all
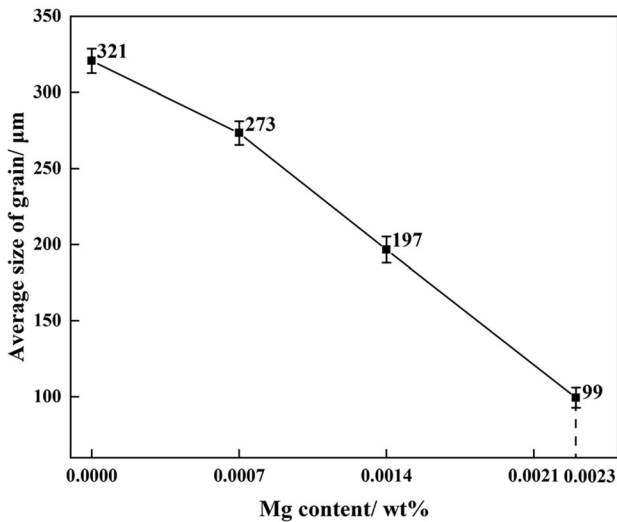
equiaxed grains, and the size of these equiaxed grains diminishes progressively with magnesium content increasing. Specifically, the average size of the equiaxed grains in the tested steels decreases from 320 to 271 μm, 195 and 101 μm as the Mg content increases from 0 to 0.0007 wt.%, 0.0014 and 0.0023 wt.%, respectively. Therefore, it can be observed that in the tested steels with Mg content of 0 to 0.0023 wt.%, the solidification structure of high-titanium high-strength steel is significantly refined with a cooling rate of 0.17 °C/s. This phenomenon is due to the evident desulfurization and deoxidation effect of Mg. The introduction of even a small amount of Mg into the melt readily reacts with residual oxygen, leading to the formation of a large number of dispersed high-melting-point oxides and magnesium-aluminate spinel. Such inclusions can increase the proportion of equiaxed crystals and promote grain refinement,[26] attributing to the decreasing critical undercooling degree and increasing nucleation-growth interval of δ-Fe after Mg treatment.[27]

TiN Morphology and Microstructure of Tested Steels with Different Magnesium Contents

The metallographic structure and TiN morphology of the central region of each tested steel with different magnesium contents are shown in Fig. 6. From Fig. 6a, the microstructure of the No. 1 steel consisted mainly of coarse-grained polygonal ferrite and pearlite with large polygonal TiN particles with sharp edges in the matrix. As the magnesium content increases from 0 to 0.0007 wt.%, 0.0014 and 0.0023 wt.%, there is a significant reduction in polygonal ferrite and pearlite size of the tested steel structure, while acicular ferrite (AF) emerges concurrently. This phenomenon is likely due to the following reasons: on the one hand, the high-titanium content in the steel, which

Figure 4. Macro-solidification structures of cylindrical samples with different contents of Mg: (a) 0 wt.% Mg; (b) 0.0007 wt.% Mg; (c) 0.0014 wt.% Mg; (d) 0.0023 wt.% Mg.

Figure 5. Statistical results of the average equiaxed grain size for tested steels with different Mg contents.

readily binds with carbon and nitrogen to form carbonitrides, effectively impedes the diffusion of carbon and the precipitation of carbides; on the other hand, the addition of Mg leads to the formation of numerous fine acicular ferrites. An increasing Mg content results in more TiN precipitates while reducing their size, further increasing the acicular ferrite quantity. These fine ferrites can effectively slice through and refine the large ferritic grains.[28,29] Additionally, the main reason for the apparent increase in the number of TiN precipitates and the reduction in their size in the central region of tested steels is likely due to the increased levels of microalloying solutes Ti and N in the steel with higher Mg contents. This increase creates a higher supersaturation and makes it easier to reach the nucleation undercooling of TiN, thus increasing the driving force for TiN nucleation, making precipitation easier.[30]

The microstructure and TiN morphology in the central region of tested steels with different Mg contents were investigated. As shown in Figs. 7, 8 and 9, scanning electron microscopy revealed many Al_2O_3–TiN composite inclusions, MgO–TiN composite inclusions and $MgAl_2O_4$–

TiN composite inclusions in the central region of tested steels. All three types of heterogeneous cores are less than 1 μm. In Fig. 7a, c, e, g, the sizes of heterogeneous nucleated cores such as Al_2O_3, MgO and $MgAl_2O_4$ are 0.68, 0.42, 0.34 and 0.44 μm, respectively. The single-TiN particles are defined as single TiN, and the TiN particles with other inclusions in the interior or edge are defined as composite TiN. The Al_2O_3 surfaces facilitate heterogeneous nucleation, leading to the formation of Al_2O_3-TiN composite inclusions.[31] The MgO, $MgAl_2O_4$ and TiN all exhibit a face-centered hexagonal crystal system. The mismatch between them can be calculated using Eqn. (12), where s and n represent the substrate and nucleating phase, respectively.[32] The (hkl), [uvw] and d[uvw] represent a low-index crystal plane in the substrate or nucleating phase, a low-index direction on the (hkl) crystal plane, and the interatomic spacing along the [uvw] direction, respectively. The θ represents the angle between [uvw]s and [uvw]n. According to Eqn. (12) and the relevant data in Table 3, the mismatch between MgO and TiN can be calculated as 0.02%, while the mismatch between $MgAl_2O_4$ and TiN is only 5.03%. Generally, when the mismatch between the two phases is less than 12%, the first precipitated compound phase can act as a non-spontaneous nucleus to promote nucleation. The high-melting-point MgO and $MgAl_2O_4$ preferentially precipitate and can serve as a heterogeneous nucleating core for TiN due to its low mismatch with TiN. During the solidification process, Ti segregation results in significantly higher Ti concentrations at the solidification front far exceeding the critical Ti concentration required for the heterogeneous nucleation of TiN.[31] Consequently, TiN readily nucleates around MgO and $MgAl_2O_4$ cores in large quantities during solidification (Tables 4 and 5).

$$\delta_{(hkl)_n}^{(hkl)_s} = \sum_{i=1}^{3} \left[\frac{\left| d_{[uvw]_s}^i \cos \theta - d_{[uvw]_n}^i \right|}{d_{[uvw]_n}^i} \right] \times \frac{1}{3} \times 100\%$$

Eqn. 12
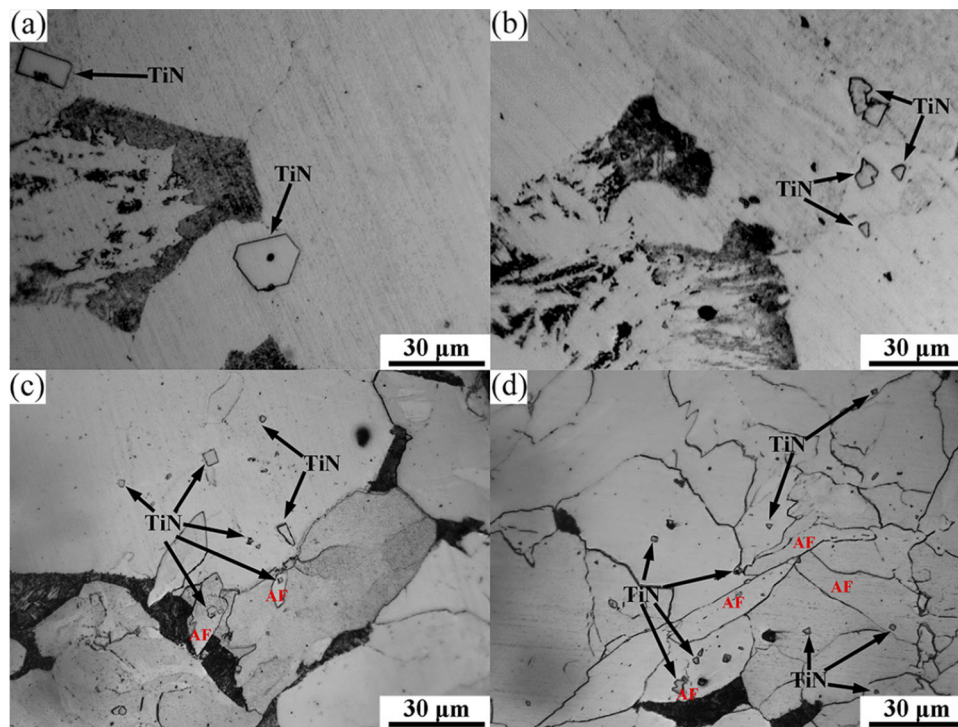
Figure 6. Typical metallographic morphology of TiN in the tested steels with different Mg contents at 500× magnification: (a) 0 wt.% Mg; (b) 0.0007 wt.% Mg; (c) 0.0014 wt.% Mg; (d) 0.0023 wt.% Mg.

Quantity, Size and Precipitation Location of TiN (≥ 1 μm) in the Central Region of Tested Steels with Different Magnesium Contents

The statistical results of the quantity, size and precipitation location of TiN (≥ 1 μm) in the central region of tested steels with different Mg contents are shown in Fig. 10. From Fig. 10a–d, in the central region of No. 1 steel (0 wt.% Mg), the size of TiN particles is primarily concentrated in the range of 5–15 μm, with a higher density in the 5–12 μm range (density of TiN 44.4 No./mm^2). For the tested steels with Mg content ranging from 0.0007 to 0.0023 wt.%, there was a sharp increase in density of TiN (density of TiN 102.4–129.4 and 144.2 No./mm^2). The size distribution mainly ranged between 1–8 μm, with higher densities observed within the range of 1–5 μm. No large-sized TiN particles exceeding 12 μm were found, and single TiN exhibited significantly higher densities than composite-TiN in four tested steels. As shown in Fig. 10e, the maximum size of TiN in the central region of tested steels changes from 16.5 to 10.4 μm, 9.8 and 9.3 μm as the Mg content increases from 0 to 0.0007 wt.%, 0.0014 and 0.0023 wt.%, respectively. The average size of TiN decreases from 9.1 to 4.2 μm, 3.3 and 3.1 μm, respectively. The precipitation of TiN in the central region of tested steel is mainly observed at grain interior, with a decrease in proportion precipitated at grain boundaries with increasing Mg content, ranging from 22.7 to 16.8%, 14.5 and 14.8%. The main reason is that larger grain interior area compare

to the grain boundary area. Ti and N atoms diffuse, aggregate and continuously diffuse into MgO/MgAl$_2$O$_4$, creating more space and nucleation points at solidification defects. Thereby, TiN nucleation propensity is further heightened at grain interior.[34]

Nucleation and Growth Mechanisms of TiN in the Central Region of Tested steels During Solidification Cooling Process

The nucleation, growth and aggregation processes of TiN in the solid-liquid two-phase region of Nos. 1–4 steels with different Mg contents are shown in Fig. 11. Owing to the equilibrium partition coefficients of Ti and N atoms in solid and liquid phases being significantly less than 1, the solubility of Ti and N in the δ-phase is markedly lower than that in the liquid phase.[35] Due to a consistently low cooling rate (0.17 °C/s) in four tested steels, heat dissipation in the central region of tested steels lacks directionality, allowing grain to grow freely within the liquid phase at similar rates on all sides. This results in the growth of δ equiaxed grains during solidification. In the nucleation and growth processes of the δ equiaxed grains at the solidification front, as both TiN and δ-phase belong to cubic crystal systems, δ equiaxial grains readily form on the surface of TiN particles due to their favorable lattice mismatch relationship with δ-Fe (3.9% at 1538 °C).[19,36] The formation of these equiaxial grains contributes to refine grain size within the
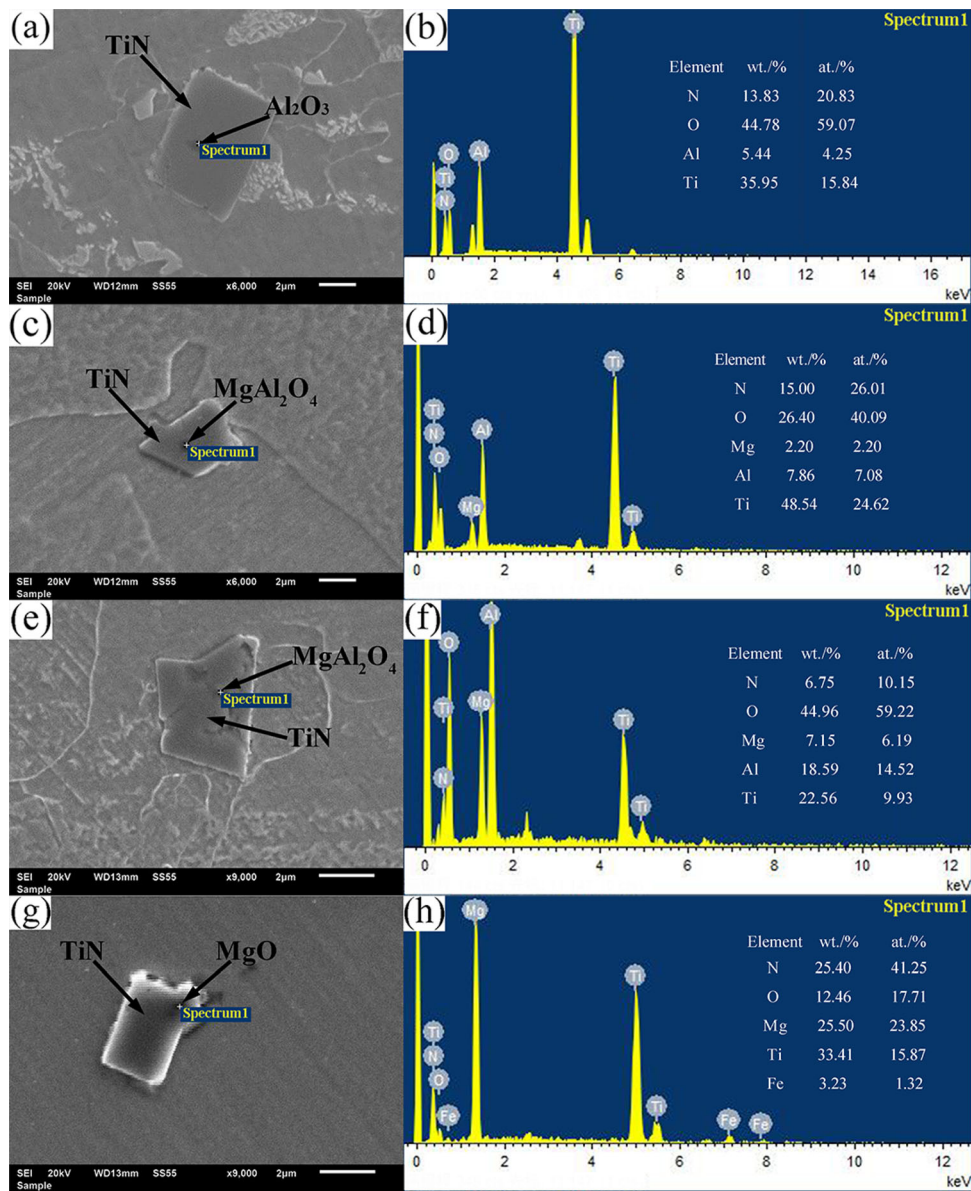
Figure 7. Morphologies and energy spectrum analysis of composite TiN in the tested steels with varying Mg contents: (a, b) 0 wt.% Mg; (c, d) 0.0007 wt.% Mg; (e, f) 0.0014 wt.% Mg; (g, h) 0.0023 wt.% Mg.

δ-phase. With the addition of Mg, the rapid vaporization of Mg in molten steel forms small bubbles that stir the molten steel during their rise and swiftly generate fine $MgAl_2O_4$ or MgO inclusions. Due to the favorable interface wetting characteristics of TiN and $MgO/MgAl_2O_4$, as well as the minimal lattice mismatch between TiN and $MgO/MgAl_2O_4$, the presence of MgO and $MgAl_2O_4$ in molten steel can enhance the nucleation rate of TiN. This leads to easier attainment of the critical concentration required for TiN nucleation around nucleating particles by facilitating a higher concentration of Ti and N atoms. Consequently, the growth driving force acting on individual TiN particles diminishes, resulting in an overall reduction in both average and maximum size of TiN growth. With the increase in Mg content in the tested steels, a higher amount of MgO

and $MgAl_2O_4$ were introduced as nucleation particles, thereby inducing a significant number of spontaneous TiN nucleation and heterogeneous nucleation with MgO and $MgAl_2O_4$ as the core. It leads to the enhancement of the nucleation rate of δ equiaxed grains. When there is a more significant number of free δ equiaxed grains at the solidification front, more TiN inclusions form within δ equiaxed grains. During δ equiaxed grains growth process, they easily connect with other equiaxed grain arms, resulting in more closed liquid phase regions. This reduces mutual flow and mixing between equiaxed crystal melts, effectively hindering migration and enrichment of Ti and N atoms in the liquid phase. Consequently, in comparison to coarse equiaxed grains, fine equiaxed grains have the ability to generate segregation regions with lower concentrations of
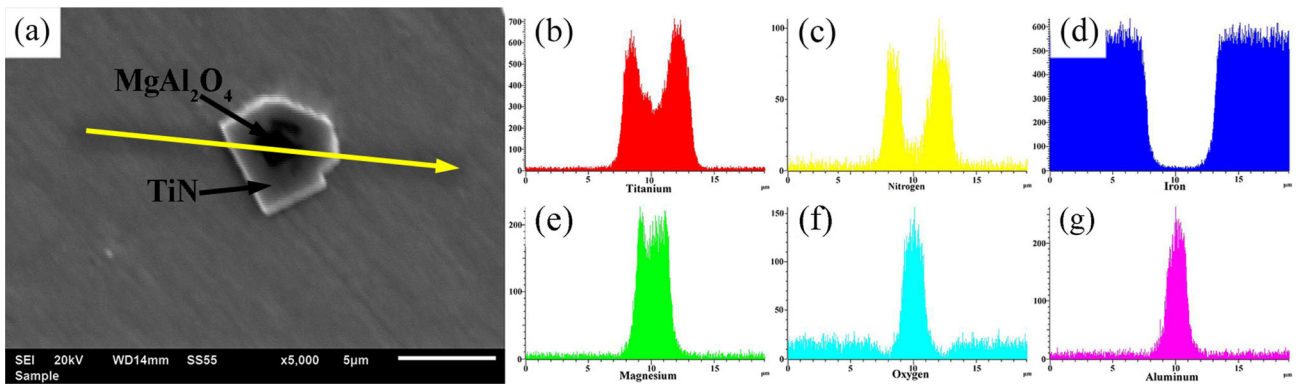
Figure 8. Morphology and line scanning analysis of MgAl₂O₄–TiN composite inclusions in 0.0023 wt.% Mg steel: (a) SEM morphology; (b) Ti spectrum; (c) N spectrum; (d) Fe spectrum; e Mg spectrum; (f) O spectrum; (g) Al spectrum.
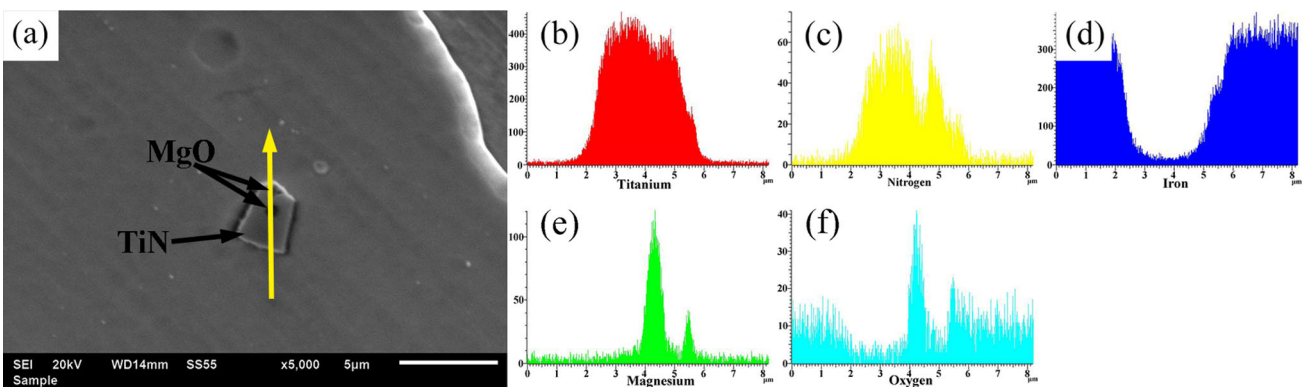
Figure 9. Morphology and line scanning analysis of MgO–TiN composite inclusions in 0.0023 wt.% Mg steel: (a) SEM morphology; (b) Ti spectrum; (c) N spectrum; (d) Fe spectrum; € Mg spectrum; (f) O spectrum.

Table 3. Crystallographic Parameters of MgO, MgAl₂O₄ and TiN[33]

Nucleate phase	Lattice structure	Lattice parameter(10^{-10} m) a
MgO	Face-centered hexagonal crystal system	4.302
MgAl₂O₄	Face-centered hexagonal crystal system	8.177
TiN	Face-centered hexagonal crystal system	4.305

Table 4. Calculation Results of Mismatch Degree Between (111) Surface of MgO and (111) Surface of TiN

MgO//TiN	$[uvw]_s$	$[uvw]_n$	$d_{[uvw]s}$	$d_{[uvw]n}$	$\theta/°$	Δ
(111)MgO	$[\bar{1}10]$	$[\bar{1}10]$	0.3045	0.3044	0	0.02%
//(111)TiN	$[\bar{2}11]$	$[\bar{2}11]$	0.5274	0.5273	0	
	$[\bar{1}01]$	$[\bar{1}01]$	0.3045	0.3044	0	

Ti and N atoms during growth. This minimizes solidification center Ti and N segregation while avoiding the formation of large-sized TiN particles. In subsequent $\delta \rightarrow \gamma$ phase transition and slow cooling processes of γ-phase, an increased presence of small -sized MgAl₂O₄ and TiN particles hinders grain growth due to their strong pinning effect on grain boundaries. The resulting grain boundary area is also increased. The barrier effect of the grain boundary can effectively impede the diffusion of Ti and N atoms across boundaries, thereby inhibiting the continuous

growth of TiN. Therefore, as the Mg content in steel changes from 0 to 0.0007 wt.%, 0.00014 and 0.0023 wt.%, density of single TiN and composite TiN gradually increase for tested steels, meanwhile maximum size of TiN and average size of TiN decrease.

Conclusion

(1) According to the thermodynamic analysis of deoxidation products in molten steel, the deoxidation products of magnesium and aluminum can be categorized into three intervals: the

**Table 5. Calculation Results of Mismatch Degree Between (111) Surface of MgAl₂O₄ and (111) Surface of TiN**

MgAl₂O₄//TiN	[uvw]s	[uvw]n	d[uvw]s	d[uvw]n	θ/°	δ
(111)MgAl₂O₄//(111)TiN	[$\bar{1}$10]	[$\bar{1}$10]	5.782	6.088	0	5.03%
	[$\bar{2}$11]	[$\bar{2}$11]	10.014	10.545	0	
	[$\bar{1}$01]	[$\bar{1}$01]	5.782	6.088	0	
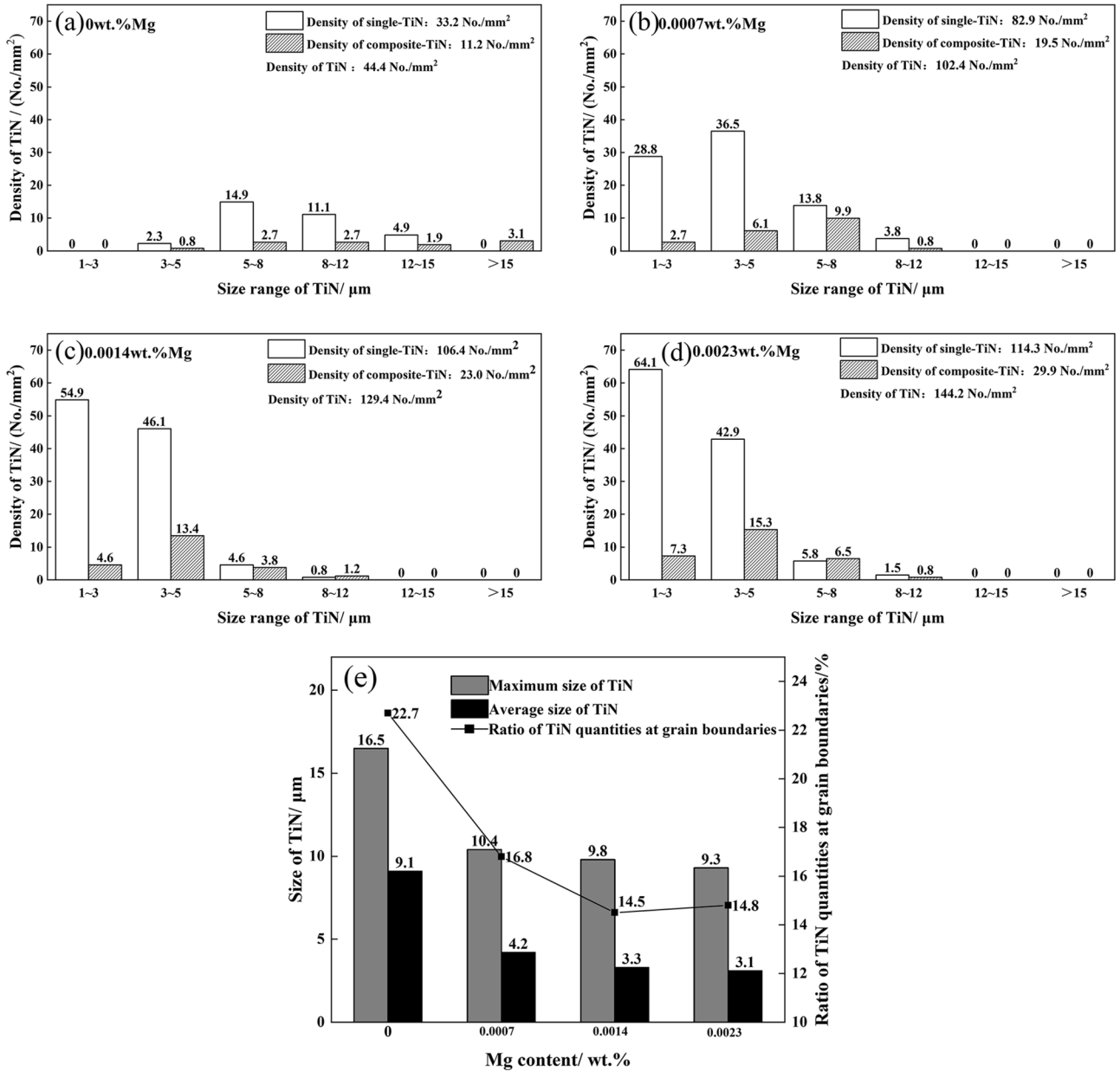
Figure 10. Statistics of single-TiN and composite-TiN density and size in tested steels at different Mg contents: (a) 0 wt.% Mg; (b) 0.0007 wt.% Mg; (c) 0.0014 wt.% Mg; (d) 0.0023 wt.% Mg; (e) Maximum and average sizes of TiN.

Al_2O_3 interval, the $MgAl_2O_4$ interval and the MgO interval. Among these intervals, the formation range of $MgAl_2O_4$ is wider, and it can be formed even with a trace amount of magnesium present. In the tested steels containing 0.0007 wt.% Mg and 0.0014 wt.% Mg, $MgAl_2O_4$ forms at $[\%Mg] \geq 3.347 \times 10^{-4} [\%Al]$; in the tested steel with 0.0023 wt.% Mg content, $MgAl_2O_4$ and MgO form at $[\%Mg] \geq 1.253 \times 10^{-2} [\%Al]$.
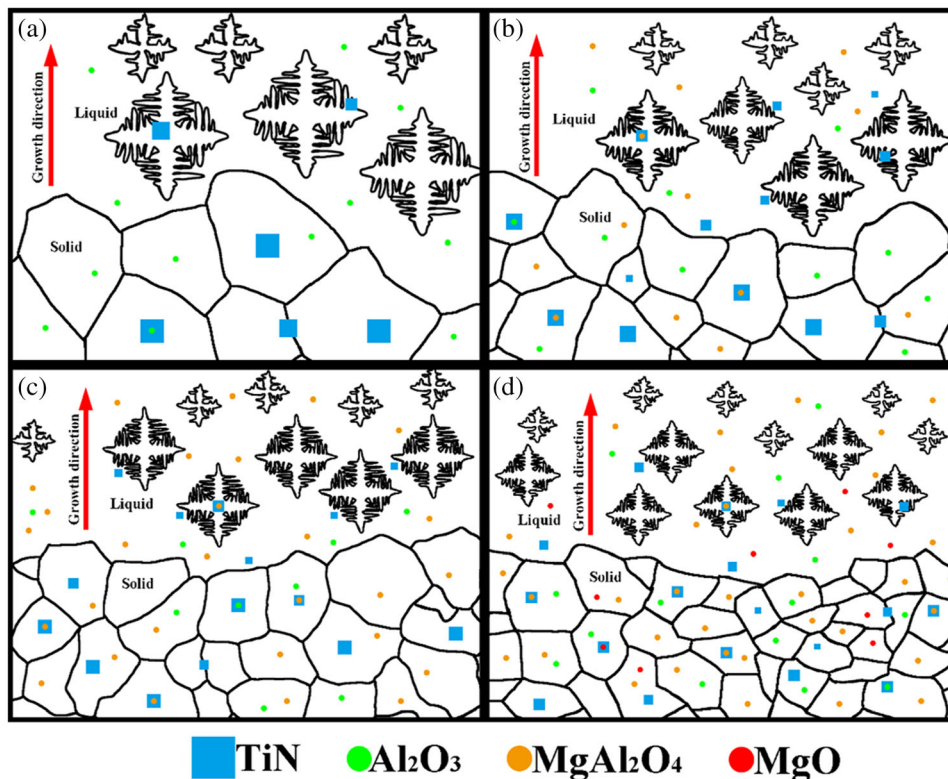
Figure 11. *Schematic of equiaxed grains formation and TiN nucleation and growth during the solidification process in tested steels with different Mg contents: (a) 0 wt.% Mg; (b) 0.0007 wt.% Mg; (c) 0.0014 wt.% Mg; (d) 0.0023 wt.% Mg.*

(2) The tested steels exhibit equiaxed grains when the solidification rate is 0.17 °C/s. The average size of equiaxed grains in each tested steel varies from 320 to 271 μm, 195 and 101 μm as the Mg contents change from 0 to 0.0007 wt.%, 0.00014 and 0.0023 wt.%.

(3) In No. 1 steel (0 wt.% Mg), composite-TiN particles are primarily Al_2O_3–TiN. As Mg content increases from 0.0007 to 0.0014 wt.% and 0.0023 wt.%, composite-TiN particles primarily consist of $MgAl_2O_4$–TiN and MgO–TiN. Calculations indicate that the small lattice mismatch between $MgAl_2O_4$ (5.03%) and MgO (0.02%) with TiN is the main reason for their role in heterogeneous nucleation of TiN. In the the No. 1 steel (0 wt.% Mg), TiN particle sizes are concentrated between 5–15 μm, with the highest precipitation density in the 5–12 μm range. In contrast, the No. 2 –No. 4 steels show a significantly higher total density of TiN precipitates, with sizes mainly ranging from 1–5 μm.

(4) As Mg content in the tested steels increases from 0 to 0.0007 wt.%, 0.0014 and 0.0023 wt.%, the total areal density of TiN precipitates in the tested steels rises from 44.4 to 102.4 No./mm^2, 129.4 and 144.2 No./mm^2. The maximum size of TiN decreases from 16.5 to 10.4 μm, 9.8 and 9.3 μm, and the average size of TiN reduces from 9.1 to 4.2 μm, 3.3 and 3.1 μm.

REFERENCES

1. R.M. Geng, J. Li, C.B. Shi et al., Effect of Ce on microstructures, carbides and mechanical properties in simulated coarse-grained heat-affected zone of 800-MPa high-strength low-alloy steel. Mater. Sci. Eng. A **840**, 142919 (2022). https://doi.org/10.1016/j.msea.2022.142919

2. J.H. Jang, C.H. Lee, Y.U. Heo et al., Stability of (Ti, M)C (M=Nb, V, Mo and W) carbide in steels using first-principles calculations. Acta Mater. **60**, 208–217 (2012). https://doi.org/10.1016/j.actamat.2011.09.051

3. X.L. Li, Z.D. Wang, Interphase precipitation behavior of carbides in Low carbon microalloyed steels containing Nb-Ti. Acta Metall. Sin. **51**, 417–424 (2015). https://doi.org/10.11900/0412.1961.2014.00582

4. H. Ohta, H. Suito, Effects of N, C and Si Contents and MgO on Dispersion of TiN Particles in Fe-1.5 percentMn-0.05(0.15) percent C Alloy. ISIJ Int. **47**, 197–206 (2007). https://doi.org/10.2355/isijinternational.47.197

5. S.J. Chen, L.J. Li, Z.W. Peng et al., On the correlation among continuous cooling transformations, interphase precipitation and strengthening mechanism in Ti-microalloyed steel. J. Mater. Res. Technol. **10**, 580–593 (2021). https://doi.org/10.1016/j.jmrt.2020.12.048

6. L.D. Xing, J.L. Guo, X. Li et al., Control of TiN precipitation behavior in titanium-containing micro-alloyed steel. Mater. Today Commun. **25**, 101292 (2020). https://doi.org/10.1016/j.mtcomm.2020.101292

7. J. Du, C.L. Strangwood, C.L. Davis, Effect of TiN particles and grain size on the Charpy impact transition temperature in steels. Mater. Sci. Technol. **28**, 878–888 (2012). https://doi.org/10.1016/S1005-0302(12)60146-7

8. T.R. Shang, W.L. Wang, J.B. Kang et al., Precipitation behavior of TiN in solidification of 20CrMnTi under continuous casting conditions. J. Mater. Res. Technol. **24**, 3608–3627 (2023). https://doi.org/10.1016/j.jmrt.2023.03.155

9. L. Xing, M. Wang, J. Guo et al., Study onsurface longitudinal crack formation of typical hypoeutectoid steel produced on a caster with billet and slab. Metals **9**, 1269 (2019). https://doi.org/10.3390/met9121269

10. P. Ahmadian, M. Taghizadeh, The effect of non-metallic inclusion size and orientation on tensile properties of stainless steel (simulation and experiment). Metall. Mater. Eng. **26**, 43–55 (2020). https://doi.org/10.30544/471

11. M. Prikryl, A. Kroupa, G.C. Weatherly et al., Precipitation behavior in a medium carbon, Ti-V-N microalloyed steel. Metall. Mater. Trans. A **27**, 1149–1165 (1996). https://doi.org/10.1007/BF02649854

12. D.P. Zhan, H.Z. Jiang, W. Gong et al., Formation and control of titanium nitride in bearing steel. J. Proc. Eng. **9**, 238–241 (2009). https://doi.org/10.3321/j.issn:1009-606X.2009.z1.051

13. T. Liu, D.F. Chen, M.J. Long et al., Control of coarse precipitates of titanium nitride in high-strength low-alloy steel. Met. Sci. Heat Treat. **61**, 534–542 (2020). https://doi.org/10.1007/s11041-020-00477-5

14. S.K. Jo, S.H. Kim, B. Song, Thermodynamics on the formation of spinel (MgO· Al$_2$O$_3$) inclusion in liquid iron containing chromium. Metall. Mater. Trans. B **33**, 703–709 (2002). https://doi.org/10.1007/s11663-002-0023-4

15. H. Ohta, H. Suito, Calcium and magnesium deoxidation in Fe-Ni and Fe-Cr alloys equilibrated with CaO-Al$_2$O$_3$ and CaO-Al$_2$O$_3$-MgO slags. ISIJ Int. **43**, 1293–1300 (2003). https://doi.org/10.2355/isijinternational.43.1293

16. W. Yang, L.F. Zhang, X.H. Wang et al., Characteristics of inclusions in low carbon Al-killed steel during ladle furnace refining and calcium treatment. ISIJ Int. **53**, 1401–1410 (2013). https://doi.org/10.2355/isijinternational.53.1401

17. H. Wang, J. Li, C.B. Shi et al., Transformation of inclusions in H13 steel treated by calcium. Chin. J. Eng. **40**, 11–18 (2018). https://doi.org/10.13374/j.issn2095-9389.2018.s1.002

18. K. Isobe, Effect of Mg addition on solidification structure of low carbon steel. ISIJ Int. **50**, 1972–1980 (2010). https://doi.org/10.2355/isijinternational.50.1972

19. K. Ken, S. Fukumoto, G. Shigesato et al., Effect of Mg addition on equiaxed grain formation in ferritic stainless steel. ISIJ Int. **53**, 2167–2175 (2013). https://doi.org/10.2355/isijinternational.53.2167

20. Y.J. Liang, M.C. Che, *Inorganic Thermodynamics Data Book* (Northeastern University Press, Shenyang, 1993), pp.114–116

21. J.X. Chen, *Steelmaking Chart Data Book*, 2nd edn. (Metallurgical Industry Press, Beijing, 2010), pp.511–614

22. H. Itoh, M. Hino, S. Ban-Ya, Thermodynamics on the formation of spinel nonmetallic inclusion in liquid steel. Merall. Mater. Trans. B **28**, 953–956 (1997). https://doi.org/10.1007/s11663-997-0023-5

23. T. Qu, D. Wang, H. Wang et al., Thermodynamic analysis on TiN Precipitation behavior in Ti-bearing peritectic steel after magnesium treatment. J. Cent. South Univ. **27**, 3637–3651 (2020). https://doi.org/10.1007/s11771-020-4567-8

24. H.X. Huang, *Principles of Iron and Steel Metallurgy*, 4th edn. (Metallurgical Industry Press, Beijing, 2013), pp.175–181

25. H. Suito, R. Inoue, Thermodynamics on Control of Inclusions Composition in Ultra-clean Steels. ISIJ Int. **36**, 528–536 (1996). https://doi.org/10.2355/isijinternational.36.528

26. C.F. Shen, X.Y. Jiang, Y. Li, Study on formation of fine spinel inclusions from Mg treated steel. Steelmaking **25**, 52–54 (2009). LGZZ.0.2009-05-017

27. X.Z. Zhou, D.Y. Wang, J. Tian et al., TiN refinement and resultant grain refinement in magnesium-treated ultra-pure ferritic stainless steel. Mater Charact **208**, 113659 (2024). https://doi.org/10.1016/j.matchar.2024.113659

28. M.M. Song, B. Song, C.L. Hu et al., Formation of acicular ferrite in Mg treated Ti-bearing C-Mn STEEL. ISIJ Int. **55**, 1468–1473 (2015). https://doi.org/10.2355/isijinternational.55.1468

29. X.H. Yuan, Y.Y. Xiao, G.C. Wang et al., TiN inducing ferrite nucleation based on the bcc-Fe/TiN interfaces formation at atomic scale by first-principles calculation. Comp. Mater. Sci **197**, 110570 (2021). https://doi.org/10.1016/j.commatsci.2021.110570

30. C.W. Zhang, T.P. Qu, D.Y. Wang et al., Effect and mechanism of MG-Ti composite treatment on solidification structure of stainless steel. J. Iron Steel Res.

31, 661–667 (2019). https://doi.org/10.13228/j.boyuan.issn1001-0963.20180310

31. M. Wang, Y.P. Bao, H. Cui et al., Study on formation mechanism of Al_2O_3-TiN composite inclusion in IF steel. J. Iron Steel Res. **22**, 29–32 (2010). https://doi.org/10.13228/j.boyuan.issn1001-0963.2010.07.008

32. B.L. Bramfitt, The effect of carbide and nitride additions on the heterogeneous nucleation behavior of liquid iron. Merall. Mater. Trans. B **1**, 1987–1995 (1970). https://doi.org/10.1007/BF02642799

33. N. Pan, B. Song, Q.J. Zhai et al., Lattice mismatch degree theory of catalyst utility for heterogeneous nucleation of liquid steel. J. Univ. Sci. Technol. B **32**, 179–190 (2010). https://doi.org/10.13374/j.issn1001-053x.2010.02.020

34. B. Lu, Y. Li, H.Y. Wang et al., Effects of cooling rates on the solidification behavior, microstructural evolution and mechanical properties of Al–Zn–Mg–Cu alloys. J. Mater. Res. Technol. **22**, 2532–2548 (2023). https://doi.org/10.1016/j.jmrt.2022.12.082

35. N. Li, L. Wang, Z.L. Xue et al., Study of precipitation and growth processes of Ti-bearing inclusions in tire cord steel. Results Phys. **16**, 102929 (2020). https://doi.org/10.1016/j.rinp.2020.102929

36. Y. Li, D.N. Crowther, M.J.W. Green et al., The effect of vanadium and niobium on the properties and microstructure of the intercritically reheated coarse grained heat affected zone in low carbon microalloyed steels. ISIJ Int. **41**, 46–55 (2001). https://doi.org/10.2355/isijinternational.41.46